

The Correlation Between the Distribution/Size of Carbides and Electrochemical Behavior of 17Cr-1Ni Ferritic-Martensitic Stainless Steel



LI WANG, CHAOFANG DONG, QIANG YU, CHENG MAN, YABO HU, ZONGBIAO DAI, and XIAOGANG LI

The correlation between the distribution/size of carbides and corrosion resistance of 17Cr-1Ni ferritic-martensitic stainless steel after different heat treatment temperatures was investigated by transmission electron microscope, electrochemical tests, and corrosion morphology observations. The results showed that the size of the precipitated phase decreased and corrosion resistance increased with an increase in the annealing temperature. When the tempering temperature was low (290 °C), carbides precipitated mainly at the phase boundaries due to a low degree of atomic matching and higher grain boundary energy. In this case, the polarization curve had a passivation interval and the pits were mainly initiated at the phase boundary. When the tempering temperature was higher than 400 °C, the carbides gradually precipitated in the martensite laths because the accelerated diffusion of Cr healed the Cr depletion zone at phase boundary. This outcome resulted in a polarization curve that had no passivation range and uniform corrosion occurred in martensitic region.

<https://doi.org/10.1007/s11661-018-4973-9>

© The Minerals, Metals & Materials Society and ASM International 2018

I. INTRODUCTION

FERRITIC-MARTENSITIC (F/M) duplex stainless steel usually has high tensile strength up to 1200 MPa and elongation up to 25 pct due to its superior microstructure in combination with the tough ferrite phase and high hardness martensite.^[1-3] It has been widely used as fasteners for bolts, screws, and studs, but suffered from corrosion in marine environment.^[4-7]

Many studies have been conducted on the microstructure of ferritic-martensitic (F/M) duplex stainless steel with various heat treatments.^[8,9] However, the corrosion mechanism of F/M stainless steel is still unclear. Generally, localized corrosion nucleation occurs on the surface at active sites such as inclusions, precipitates and regions with weak surface films.^[10-12] Several previous studies focusing on the corrosion behavior of martensitic stainless steels have shown that the carbide interfaces as

well as Cr depletion regions in martensite have a significant influence on its corrosion resistance.^[12-14] The corrosion mechanism was explained as surface oxide film formed over Cr-depleted regions is much weaker (and not stable) than other regions, therefore leading to preferential corrosion attack. Similarly, in F/M duplex steel, there is also a clear Cr-depleted region near the carbides at phase boundary or martensitic lath boundaries because martensite is enriched with Ni and C from the transformation of austenite.^[15,16] There are several causes for carbide precipitation in steel containing martensite, (1) supersaturated carbon content in martensite; (2) lower content of chromium in martensite and (3) a low degree of atomic matching and higher grain boundary energy of martensitic lath boundaries or phase boundary.^[17-19] Meanwhile, the precipitation and dissolution of carbides could be controlled by adjusting heating temperatures due to the diffusion rate of Cr/C. It seems that heat treatment plays an important role on corrosion resistance of F/M duplex stainless steel via controlling the distribution and size of carbide precipitates. Thus, further investigations are necessary to determine the relationship between heating treatment, carbide distribution, and the corrosion resistance, and hence help designing optimal heat treatment procedure of the steel.

In this paper, the distribution and size of carbides at different annealing and tempering temperatures were observed by transmission electron microscope (TEM).

LI WANG, CHAOFANG DONG, CHENG MAN, YABO HU, and XIAOGANG LI are with the Corrosion and Protection Center, Key Laboratory for Corrosion and Protection (MOE), University of Science and Technology Beijing, Beijing 100083, P.R. China. Contact e-mail: cfdong@ustb.edu.cn QIANG YU is with the Hunan Valin Lianyuan Iron and Steel Co. Ltd, Loudi 417009, China. ZONGBIAO DAI is with the Key Laboratory for Advanced Materials of Ministry of Education, School of Materials Science and Engineering, Tsinghua University, Beijing, 100084, China.

Manuscript submitted June 11, 2018.

Article published online October 23, 2018

The corrosion behavior of F/M duplex stainless steel after different heating processes was studied using electrochemical technique and immersion test. The electrochemical behavior and corrosion morphology were analyzed to explore the correlation between heating temperature and corrosion resistance. Finally, the optimal heating treatment was proposed according to all of the experimental results.

II. EXPERIMENTAL SECTION

A. Material

The chemical composition of ferritic-martensitic (F/M) stainless steel used includes (wt pct) 0.13 C, 17.10 Cr, 1.03 Ni, 0.067 Mn, 0.013 P, and 0.015 S, with the remainder being Fe. In this study, the steel was annealed at different temperature for 0.5 h and cooled in oil, then tempered at different temperatures for 0.5 h, and cooled in air (Table I). The microstructure of the steel was observed by a stereo microscope using samples sized 10 mm × 10 mm, after polished and treated with a FeCl₃ etching agent (5 g FeCl₃ + 50 ml HCl + 50 ml H₂O). Round samples with a diameter of 3 mm were ground to 50 μm with 1000-grit SiC paper, jet polished with 5 vol pct perchloric acid + 95 vol pct acetic acid at 288 K and 30 V, observed using a G20 transmission electron microscope (TEM).

B. Corrosion Measurements

Electrochemical technique and an accelerated immersion test were used to study corrosion behavior of the F/M steel. The steel electrodes used for electrochemical measurements with dimensions of 10 mm × 10 mm × 3 mm were embedded in epoxy resin, leaving a working area of 1 cm². The working surface was subsequently ground using 1000-grit SiC paper, cleaned with distilled water and acetone, and dried in cold air. The test solution was a deaerated 3.5 pct NaCl solution prepared from distilled water and analytical-grade reagents. The electrochemical measurements were conducted on a VMP3 multi-channel electrical workstation using a conventional three-electrode electrochemical cell at room temperature. The steel electrode was used as the working electrode, a platinum plate was used as the counter-electrode, and a saturated calomel electrode (SCE) was the reference electrode. Prior to testing, the steel electrode was cathodically polarized at $-0.8V_{SCE}$ for 3 minutes to remove air-formed oxide films and then the open circuit potential (OCP) was measured for 30 minutes to allow the electrode to reach a steady state. Electrochemical impedance spectroscopy (EIS) was performed over a frequency range from 100 kHz to 10 mHz, with a 10 mV amplitude sinusoidal voltage, and analyzed using ZSimpWin software. Potentiodynamic polarization measurements were carried out at a potential scanning rate of 0.1667 mV s⁻¹.

The immersion test was conducted in a 6 pct FeCl₃ + 1 pct HCl solution, which was used to assess corrosion resistance of duplex stainless steel. Samples with

dimensions of 10 cm × 10 cm were polished and immersed in the solutions for 12 hours at 35 °C. After removal of the corrosion product, the surface morphology was characterized using a stereo microscope.

C. X-ray Photoelectron Spectroscopy (XPS) Measurements

X-ray photoelectron spectroscopy (XPS) experiments were conducted to investigate the composition variation of the passive film on samples with different microstructures. XPS samples with dimension of 10 mm × 10 mm were immersed in 3.5 pct NaCl for 12 hours and investigated using XPS with a monochromatic Al K_α radiation source and a hemispherical electron analyzer operating at pass energy of 55 eV. All the peaks were corrected with the standard peak (C1s, 285.0 eV), and fitted using XPS PEAK software.

D. Corrosion Morphology Observation

The corrosion morphology of the samples after electrochemical experiments was observed using a Quanta-250 environmental scanning electron microscope (SEM) and a laser scanning confocal microscope to characterize the initiation position of pits. The surface of the soaked specimen was observed with a stereo microscope. Transmission electron microscope (TEM) investigations were conducted to observe position and size of the precipitates.

III. RESULTS

A. Microstructural Characterization

Microstructure of the F/M steels that were treated at different annealing temperatures and tempered at 620 °C is shown in Figure 1. When tempered at a constant temperature (620 °C), the microstructure of the steel mainly consisted of ferrite matrix and martensitic islands. With the annealing temperature increasing, the volume fraction of the martensite appeared to first increasing before decreasing. When the annealing temperature was 1000 °C, the highest volume fraction of the martensite was 53.2 pct, which was consistent with results of thermodynamic calculation (Figure 2(a)) where the volume fraction of the martensite content usually had a peak value at a certain temperature (1000 °C) according to the calculated equilibrium phase diagram.^[20,21]

Figure 2(b) shows the hardness of the steels treated with different heat treatment processes. The volume fraction of martensite was measured equal to the aerial fraction calculated from OM images by 3D stereo microscope (VK9700). The samples annealed at 1000 °C had the highest hardness due to having more martensite islands. The decrease of the carbon of the solid solution in α-Fe with precipitation of carbides resulted in the decline of the hardness with the tempering temperature.^[22]

Table I. The Samples of F/M Stainless Steel by Different Heat Treatments

Samples	Annealed Temperature (°C)	Tempered Temperature (°C)
I	950	620
II	1000	290
III	1000	400
IV	1000	620
V	1050	620

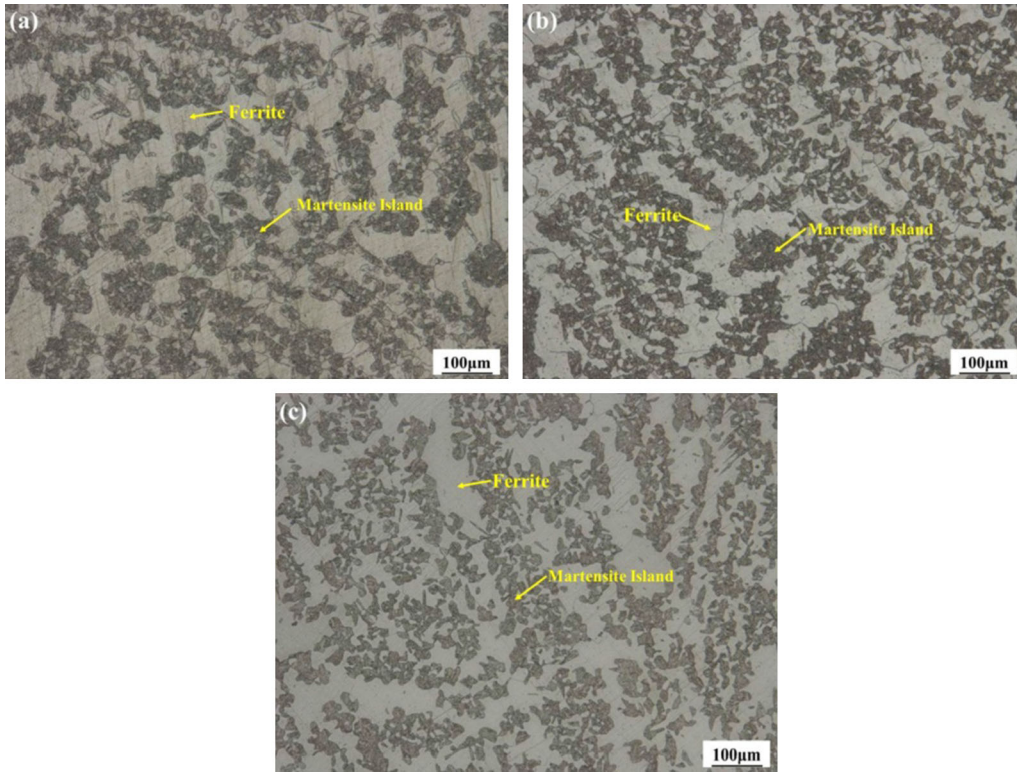


Fig. 1—Microstructures of ferritic-martensitic stainless steel: (a) annealed at 950 °C and tempered at 620 °C; (b) annealed at 1000 °C and tempered at 620 °C; (c) annealed at 1050 °C and tempered at 620 °C.

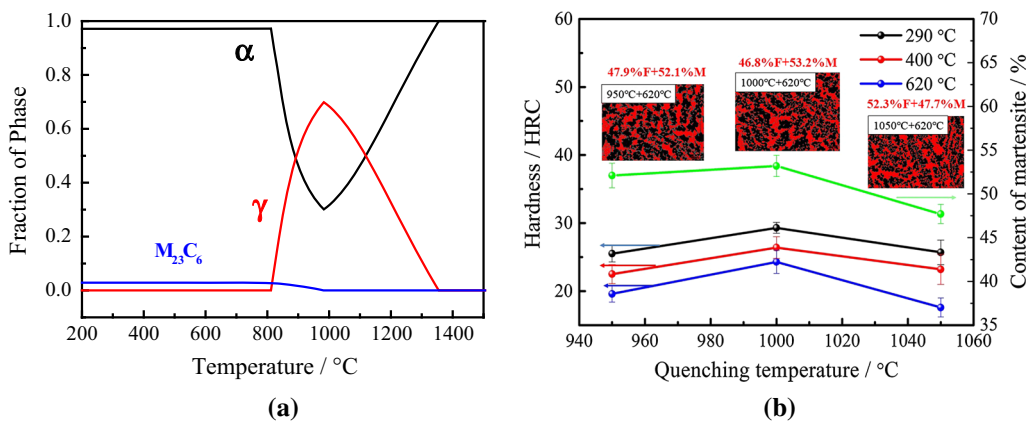


Fig. 2—Phase fractions, hardness and content of martensite at different heat treatment temperatures: (a) phase fractions as a function of temperature; (b) hardness and content of martensite.

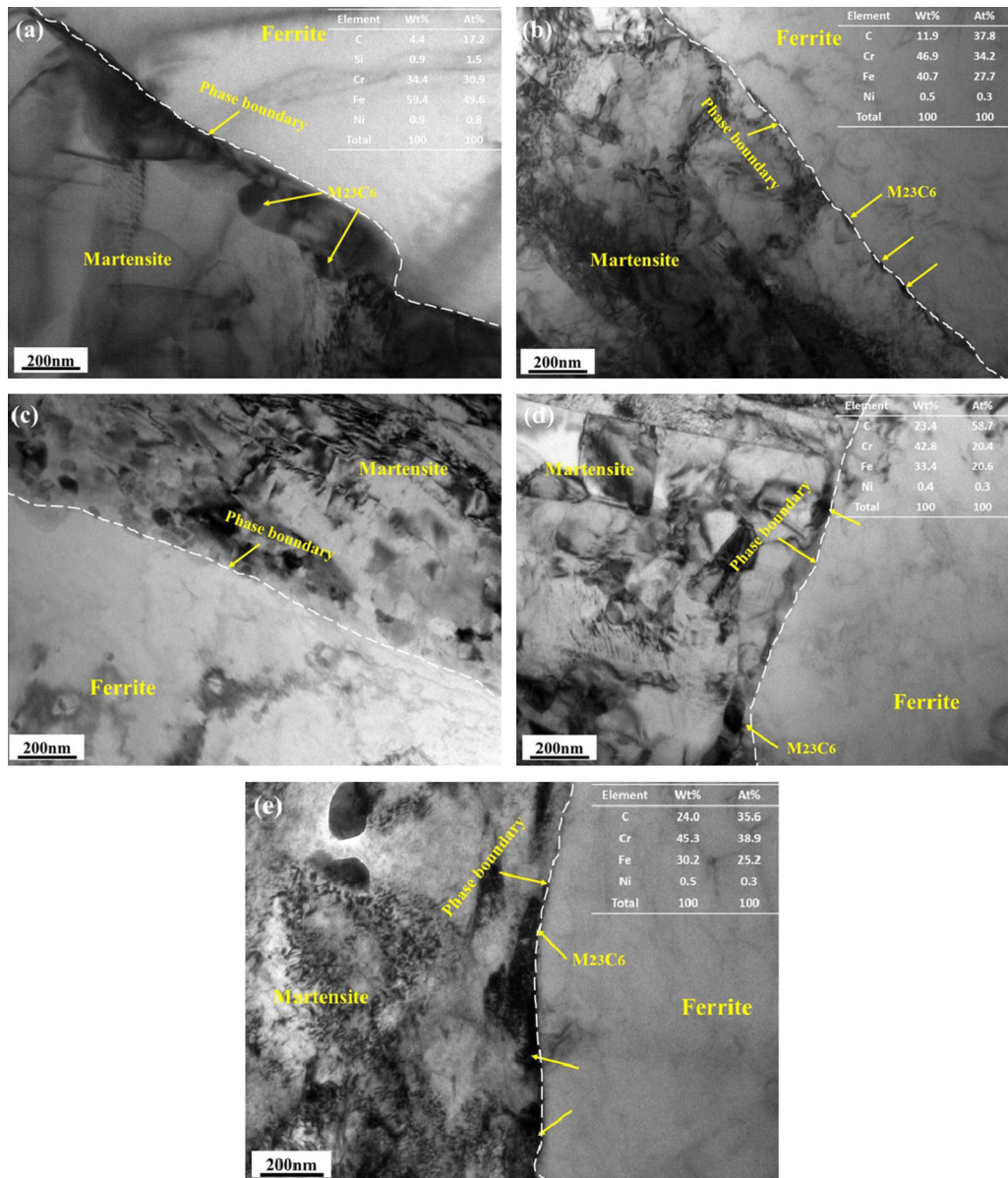


Fig. 3—TEM images of duplex steel at the phase boundary after different heat treatment processes: (a) 950 °C + 620 °C; (b) 1000 °C + 620 °C; (c) 1050 °C + 620 °C; (d) 1000 °C + 290 °C; (e) 1000 °C + 400 °C.

Figure 3 displays TEM images of the duplex steel at the phase boundaries after different heat treatments. As shown in Figure 3, some precipitates mainly consisted of Fe, Cr, and C could be clearly observed from energy dispersive spectrometer (EDS). Thus, the predominant precipitates were most likely carbides. By fixing the tempering temperature at 620 °C, the carbides in the sample annealed at 950 °C had the largest average size of 150 nm (Figure 3(a)) compared with those annealed at 1000 °C (50 nm, shown in Figure 3(b)) and 1050 °C (30 nm, shown in Figure 3(c)), indicating that the size of the precipitates decreased with increasing annealing temperature. Then, by taking different tempering temperatures (Figures 3(a), (d), and (e)) into consideration, it could be found that the size of the precipitates increased from 100 nm to 150 nm when the tempering

temperature rising from 290 °C to 400 °C. When the tempering temperature reached 620 °C, the sizes of the precipitates reduced to 50 nm. The reduction of the carbide size at 620 °C might be due to the dissolution of carbides, caused by diffusion of the Cr to depleted regions.^[14]

TEM images of carbide precipitates between martensite laths obtained after different heat treatments are shown in Figure 4. The selected area diffraction (SAD) pattern acquired from the lath interface precipitate together with TEM-EDS analysis (Figures 4(a) through (e)) confirmed that the precipitates are Cr-rich $M_{23}C_6$ -type carbides ($M = Fe, Cr$) with face-centered cubic structure. Additionally, as shown in Figures 4(a) through (c), size of the precipitates decreased with the annealing temperature increasing. Large-size

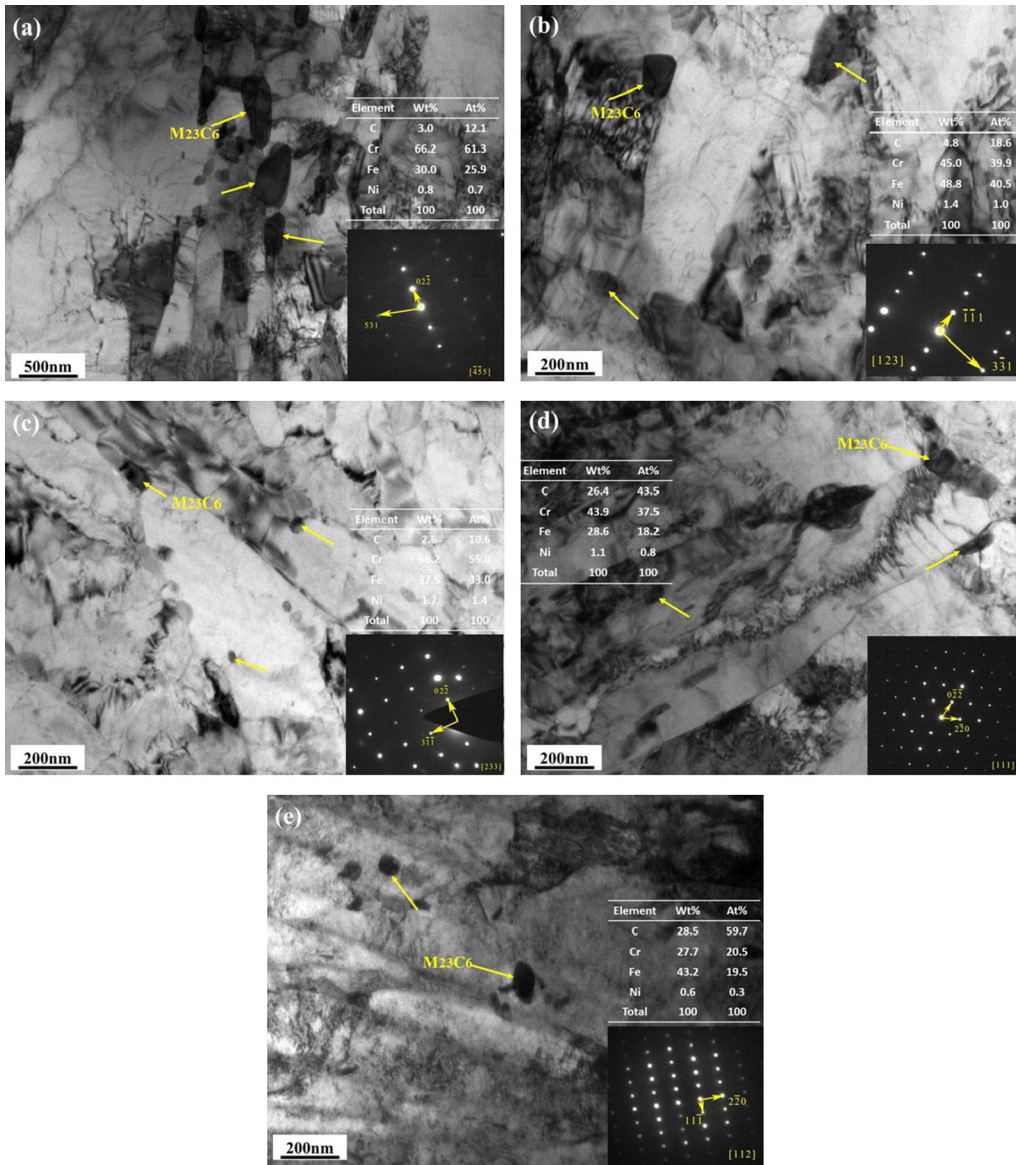


Fig. 4—TEM images of duplex steel between the martensite laths after different heat treatment processes: (a) 950 °C + 620 °C; (b) 1000 °C + 620 °C; (c) 1050 °C + 620 °C; (d) 1000 °C + 290 °C; (e) 1000 °C + 400 °C.

precipitates can only be observed at 950 °C, as shown in Figure 4(a). When the annealing temperature was raised to 1050 °C, both the amount and size of the precipitates decreased, which was consistent with the results of other studies.^[23,24] Furthermore, the effect of the tempering temperature on the carbide distribution was also investigated, as shown in Figure 4(d) and (e). When the tempering temperature was 400 °C, the size of the precipitates between martensite laths was approximately 150 nm, whereas it was only 50 nm at 290 °C. The regularity of the precipitates among martensite laths is similar with the phase boundary.^[25–27]

B. Electrochemical Behavior

Figure 5(a) shows the potentiodynamic polarization curves of F/M duplex steel after annealing at different

temperatures. It is clear that the corrosion current density became 10 times smaller when the annealing temperature increased from 950 °C to 1050 °C. Additionally, the corrosion potential (E_{corr}) also presented a monotonically increasing tendency, from $-0.36 \text{ V}_{\text{SCE}}$ to $-0.23 \text{ V}_{\text{SCE}}$, as the annealing temperature increased from 950 °C to 1050 °C. This indicates better resistance to corrosion after annealing at high temperature, most likely due to the size of the precipitated phase.^[28]

The impact of tempering temperature on the polarization curve is shown in Figure 5(b). It can be seen that the tempering temperature did not have a significant effect on the corrosion potential, but played an important role in the different extents of the passivation behavior. When the sample was tempered at 290 °C, obvious passivation behavior was observed and corrosion current density is almost constant, while no obvious

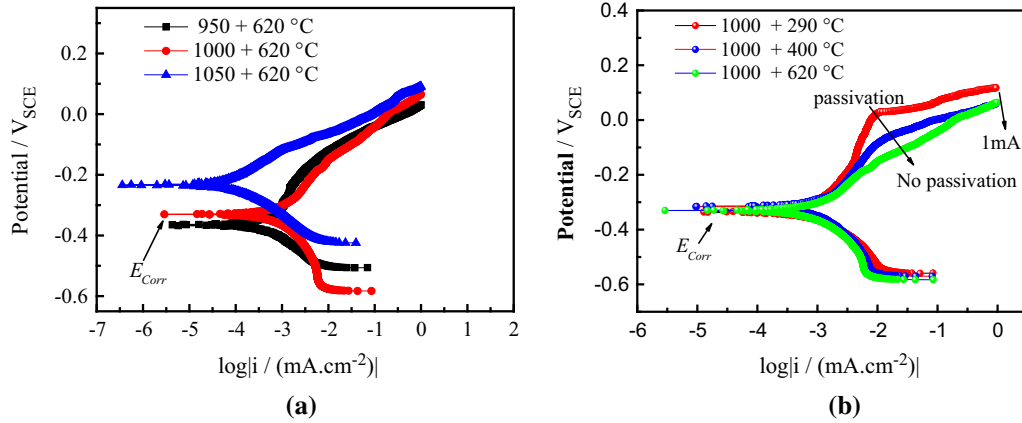


Fig. 5—Polarization curves of F/M steels in 3.5 pctNaCl solution at room temperature: (a) after different annealing temperatures; (b) after different tempering temperatures.

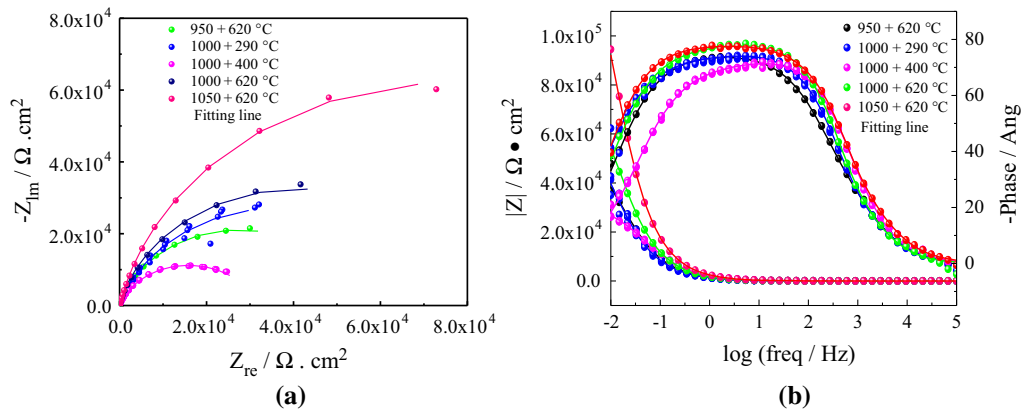


Fig. 6—Electrochemical impedance spectroscopy of duplex steels in 3.5 pctNaCl solutions: (a) Nyquist plots; (b) Bode plots.

passivation behavior was observed at 400 °C and 620 °C. The inconspicuous passive behavior, which indicates a rapid increase in current density with an increase of the polarization potential after the corrosion potential, predicts a more likely uniform corrosion as opposed to localized corrosion. This was consistent with previous results that tempering process decreased the pitting potential of martensite steel.^[29,30]

Figure 6 shows the EIS results of F/M duplex steels in a 3.5 pct NaCl solution at room temperature. Generally, the corrosion resistance of the steel was enhanced as the annealing temperature increased (950 °C + 620 °C, 1000 °C + 620 °C and 1050 °C + 620 °C in Figure 6(a)). However, when considering the tempering temperature, an unusual phenomenon appeared: the corrosion resistance was much lower at 400 °C of tempering temperature compared to that at 290 °C and 620 °C. This might reveal a different passivation behavior, which will be investigated in the future.

The equivalent circuit used to fit the EIS data is shown in Figure 7, where C_f and R_f are the capacitance and resistance of the passive film, respectively; C_{dl} is the double-layer capacitance; R_{ct} is the charge-transfer

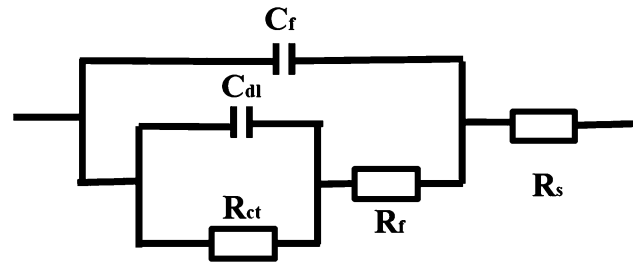


Fig. 7—The equivalent circuit diagram used to fit the EIS experimental data after different heat treatment processes.

resistance, and R_s is the solution resistance.^[31–33] All of the fitting data from the EIS analysis are presented in Table II. The sample annealed at 1050 °C and tempered at 620 °C had the largest R_{ct} value of $1.52 \times 10^5 \Omega \text{ cm}^2$. This is because the F/M duplex steel treated with higher annealing and tempering temperature had fewer and smaller precipitates according to the results of the matrix composition and the microstructure obtained from SEM and TEM.^[34]

C. Potentiostatic Polarization

In order to study the possible localized corrosion behavior of F/M duplex steel, two anodic polarization potentials were applied on the specimens. Figure 8 shows the pitting morphologies of specimens polarized at a constant potential of $0.1 V_{SCE}$ and $0.2 V_{SCE}$ for 1800 seconds in a 3.5 pct NaCl solution. SEM analysis of the surface of the specimens after potentiostatic polarization at $0.1 V_{SCE}$ for 1800 seconds showed that preferential pitting corrosion was observed at the phase boundary, as shown in Figure 8(a). This might be due to larger precipitation of nano-sized carbides with Cr depletion located on the phase boundary. Then, in order to study the extension of pitting, the cross section of the specimen was eroded and the microstructure was observed using a laser scanning confocal microscope after potentiostatic polarization at $0.2 V_{SCE}$ for 1800 seconds, as shown in Figure 8(b). It is shown that pitting corrosion mainly extended along the depth direction of the martensite, whereas the ferrite was not corroded. This may be related to the distribution of precipitates in the martensite islands,^[13] which was also consistent with the conclusion of precipitates introducing localized corrosion.

D. Immersion Test

Figure 9 shows the corrosion morphologies of different specimens with dimensions of 25 mm × 25 mm × 3 mm after immersion in a 6 pct FeCl₃ solution for 12

hours. the weight-loss rate was calculated according to Eq. [1].

$$V = \frac{G_0 - G_1}{2t \times (a \times b + a \times c + b \times c)}, \quad [1]$$

where V represents the corrosion rate, $g \text{ m}^{-2} \text{ h}^{-1}$; G_0 is the initial mass of the plate, g ; G_1 is the mass of the plate after cleaning, g ; t is the immersion time, h ; and a , b , and c are the length, width, and thickness, respectively, m . Figure 9 shows obvious difference for the corrosion behavior of the soaked samples treated at different heat treatment conditions from the surface topography. When annealed at 950 °C and 1000 °C, pitting corrosion could be observed and usually appeared on the location of martensitic islands. The corrosion rate of specimens annealed at 950 °C and 1000 °C was about 30 to 35 $g \text{ m}^{-2} \text{ h}^{-1}$. When annealed at 1050 °C, no obvious pitting corrosion was observed and the corrosion rate was about 20 $g \text{ m}^{-2} \text{ h}^{-1}$. Raising the tempering temperature also had a significant effect on the corrosion morphology. As shown in Figures 8(b), (d), and (e), specimens tempered at 400 °C suffered from the most serious corrosion compared to that tempered at 290 °C and 620 °C, which was consistent with the EIS results shown in Figure 6.^[35,36]

E. Characterization of the Surface Film

The corrosion resistance of stainless steel is usually related to the passive film formed on the surface. The above discussion confirmed that the microstructure was

Table II. Electrochemical Impedance Spectrum Fitting Data

Heat Treatment Temperature (°C)	R_s ($\Omega \text{ cm}^2$)	C_f ($F \text{ cm}^{-2}$)	R_f ($\Omega \text{ cm}^2$)	C_{dl} ($F \text{ cm}^{-2}$)	R_{ct} ($\Omega \text{ cm}^2$)
950 + 620	9.197	7.852×10^{-5}	20.55	7.081×10^{-5}	5.498×10^4
1000 + 290	6.98	2.204×10^{-5}	3.553	1.448×10^{-4}	7.386×10^4
1000 + 400	9.242	8.667×10^{-5}	3.722	3.139×10^{-5}	2.852×10^4
1000 + 620	6.789	2.537×10^{-5}	4.46	9.558×10^{-5}	8.311×10^4
1050 + 620	7.431	5.332×10^{-5}	12.04	2.886×10^{-5}	1.522×10^5

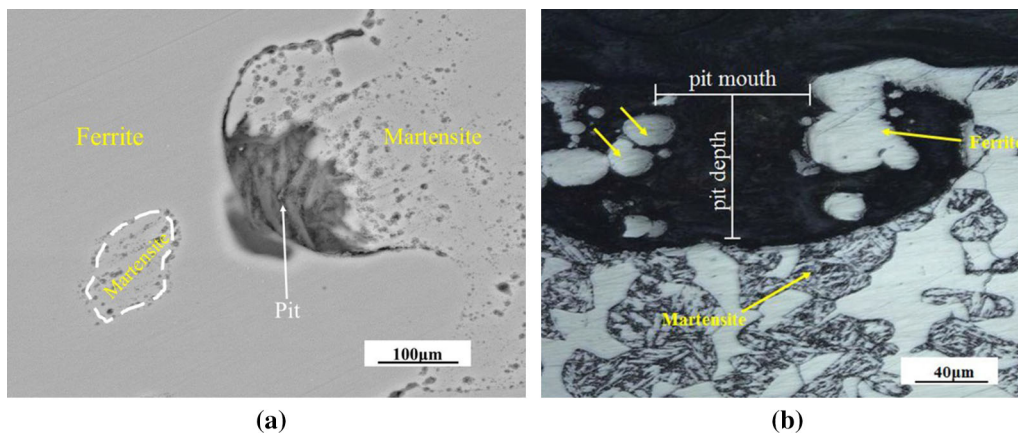


Fig. 8—Corrosion morphology of F/M steel after potentiostatic polarization at (a) $0.1 V_{SCE}$ and (b) $0.2 V_{SCE}$ for 1800 s in 3.5 pct NaCl solution.

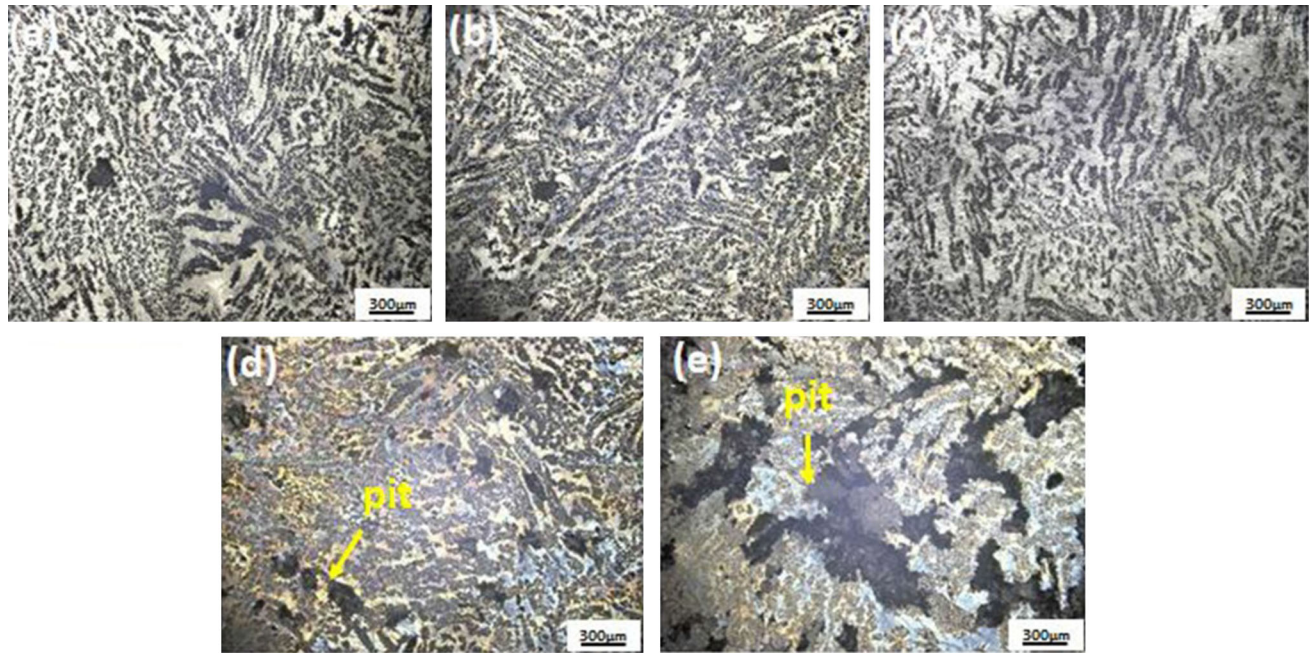


Fig. 9—Surface morphology of duplex steel after immersion experiment for 12 h in 6 pct FeCl_3 solution at room temperature: (a) 950 °C + 620 °C; (b) 1000 °C + 620 °C; (c) 1050 °C + 620 °C; (d) 1000 °C + 290 °C; (e) 1000 °C + 400 °C.

significantly changed by different heat treatment processes, thereby further modifying the surface composition of the passive film. The composition of the surface film on the duplex steel after immersion in 3.5 pct NaCl for 12 hours was analyzed by XPS. As shown in Figure 10, the passive film mainly consisted of Fe, Cr, and O, but no obvious Ni and Cl was observed. It is shown that the composition of the passive film mainly contained FeO (709.5 eV), Fe_2O_3 (710.5 eV), FeOOH (711.6 eV), Cr_2O_3 (575.9 eV), $\text{Cr}(\text{OH})_3$ (576.6 eV), and CrO_3 (577.7 eV),^[37,38] as shown in Table III. The content of FeOOH and Cr_2O_3 in the passive film increased with increasing of annealing temperatures, where Cr_2O_3 is the most chemically stable amorphous oxide and can improve the corrosion resistance of the passive film.^[39,40]

The iron and chromium contents in the passive film obtained after different temperatures were calculated based on their corresponding peak areas. As shown in Figure 11, the ratio of Fe/Cr formed at low annealing temperature (950 °C) was about 2.1, while after high annealing temperature (1050 °C), the ratio was about 1.1. The Fe/Cr ratios in the passive films after different temperatures indicated that Cr was enriched after high-temperature annealing in the passive film. The Fe/Cr ratios also confirmed that oxidation of Cr (III) increased at high temperatures (1050 °C). The higher Cr_2O_3 content and low ratio of Fe/Cr in the passive film of the high-temperature annealing condition might be attributed to less and smaller precipitation of Cr-rich carbides that appeared during the annealing treatment at 1050 °C, thus increasing the Cr content in the matrix.^[41]

IV. DISCUSSION

Many studies^[13,14,31] have shown that Cr-rich precipitates in stainless steel are harmful to the corrosion resistance of the steel because they introduce a Cr-depleted zone into the structure. Figure 12 shows the variation curve of the Cr concentration at the carbide–matrix interface regions of the specimens after annealing at 1000 °C and tempering at 290 °C. The Cr content in the F/M stainless steel and M_{23}C_6 carbide was approximately 17.1 and 56 pct, respectively, as shown in Figure 11. However, the measured Cr-depleted zone at the phase boundary only contained 15.5 pct Cr with a width of 25 nm. The lower concentration of Cr would lead to the formation of a weak passive film in the Cr-depleted zones. Aggressive ions could easily penetrate through the passive film and act as a precursor for pit nucleation. In the present work, it was obvious that the Cr-depleted zones were distributed around Cr-rich M_{23}C_6 carbides, which most likely precipitated during the annealing or tempering treatment processes. Thus, the formation of a protective passive film (mainly formed by chromium oxides) over the Cr-depleted zones was limited owing to the deficiency of Cr. Then, pitting nucleation occurred in the unprotected region and gradually expanded to contact nearby smaller carbides in some aggressive-ion-containing environments (Figure 13).

The relationship between corrosion behavior and heat treatment conditions is summarized in Table IV and Figure 14. When the tempering temperature is lower (290 °C), the carbides preferentially precipitated at the phase boundary other than martensite lath owing to the

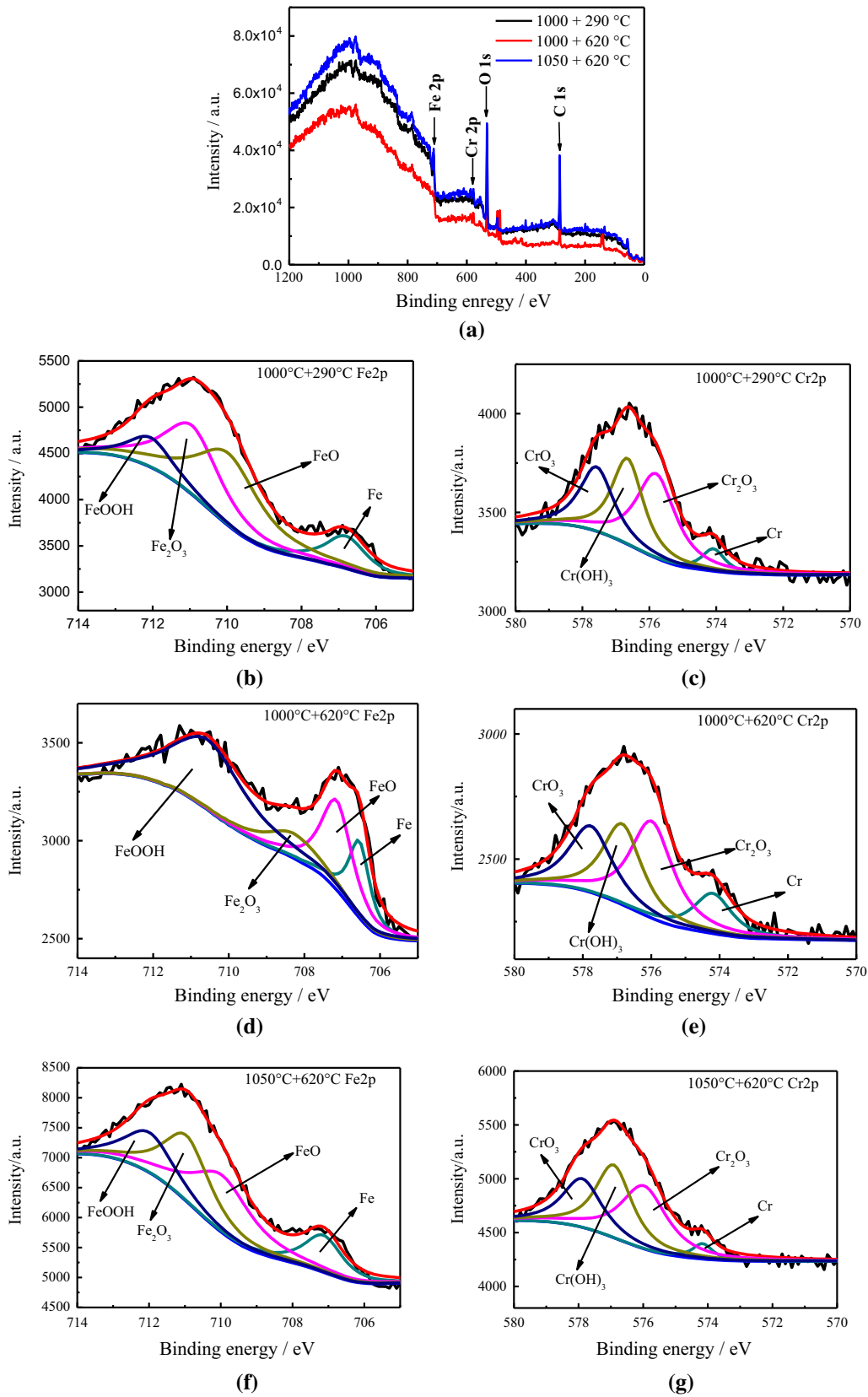


Fig. 10—XPS spectra of the surface film formed on duplex steel after immersion experiment for 12 h in 3.5 pct NaCl solution at room temperature: (a) survey; (b) Fe2p of 1000 °C + 290 °C; (c) Cr2p of 1000 °C + 290 °C; (d) Fe2p of 1000 °C + 620 °C; (e) Cr2p of 1000 °C + 620 °C; (f) Fe2p of 1050 °C + 620 °C; (g) Cr2p of 1050 °C + 620 °C.

Table III. Binding Energy, Compounds, and Compounds Content Extracted from XPS Analysis

Element	Compounds	Binding Energy (eV)	Compounds Content (1000 °C + 290 °C) (Pct)	Compounds Content (1000 °C + 620 °C) (Pct)	Compounds Content (1050 °C + 620 °C) (Pct)
Fe 2p	Fe	706.9	16.7	11.7	16.6
	FeO	709.5	19.7	21.5	23.9
	Fe ₂ O ₃	710.5	34.2	36.7	10.9
	FeOOH	711.6	29.4	30.1	48.6
Cr 2p	Cr	574.1	5.2	13.0	4.0
	Cr ₂ O ₃	575.9	28.4	35.2	37.3
	Cr (OH) ₃	576.6	35.9	27.2	34.4
	CrO ₃	577.7	30.5	24.6	24.3

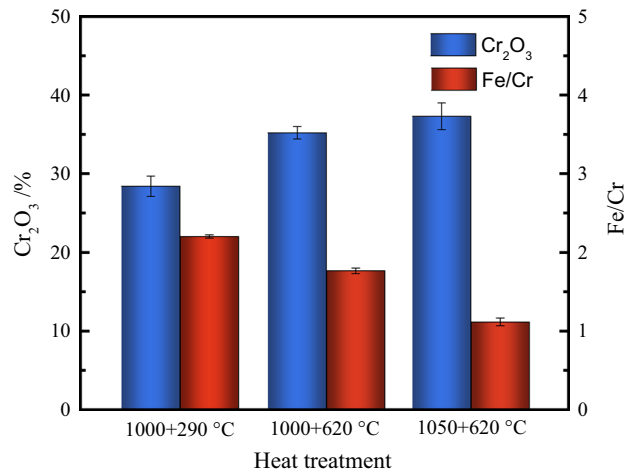


Fig. 11—The Cr₂O₃ and Fe/Cr of passive films after different temperatures.

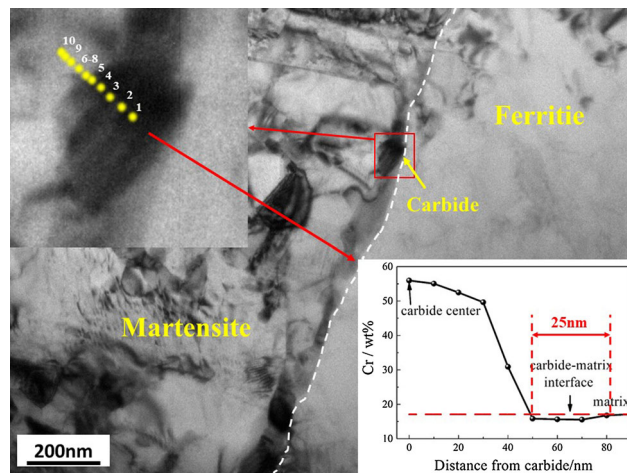


Fig. 12—Cr concentration profiles of carbide-matrix interface regions.

low degree of atomic matching and the higher grain boundary energy. In this case, the passive film that formed on the F/M steel was relatively complete due to the high density distribution of the precipitated phase (dispersion distribution with small size) without local coarsening. Thus, the potentiodynamic polarization

curve showed an obvious passivation interval and pits mainly initiated at the phase boundary because of Cr depletion in the vicinity of larger precipitates, as shown in Figure 8(a).

However, when the tempering temperature increased to 400 °C, the precipitated phase at the phase boundary and the martensite lath had almost the same size (about 150 nm). The polarization curve had a weak passivation range, and the corrosion morphology exhibited uniform corrosion and pitting corrosion. When the tempering temperature was high (600 °C), the carbides at the phase boundary began to diffuse to the matrix and leading to the gradual disappearance of the Cr-depleted zone near the carbide at the boundary. Carbides were gradually separated from the martensite laths with increasing tempering temperature. When the size of the precipitates between martensite laths was larger than that at the phase boundary, it was difficult to form compact and stable passive films on the surface of the martensite region owing to the extensive distribution of nano-sized carbides with serious Cr depletion at the martensitic lath interfaces.^[13,14] Thus, the passive film could not protect the steel substrate from corrosion by a corrosive medium such as Cl⁻. At this condition, no passivation interval was observed in the polarization curve and uniform corrosion occurred in the martensite phase through the immersion experiments as shown in Figure 9(e). The results were well matched with those of the potentiodynamic polarization tests (Figure 5), indicating that no effective passive films could be formed on the surface of the F/M steels tempered at 400 °C and 620 °C.

In the present work, after evaluating the effect of heat treatment temperature on electrochemical behavior of F/M steel, it was shown that with the annealed temperature increasing, the size of carbides gradually decreased and the corrosion resistance increased. With the increasing of tempering temperature, the carbides gradually precipitated between the martensite laths and dissolved at the phase boundary because of the Cr diffusion to Cr-depleted areas. The passivation phenomenon became less obvious. In order to improve corrosion resistance of the steel, a better heat treatment process for the F/M duplex stainless steel is annealed at high temperature (1050 °C) and tempered at low temperature (290 °C).

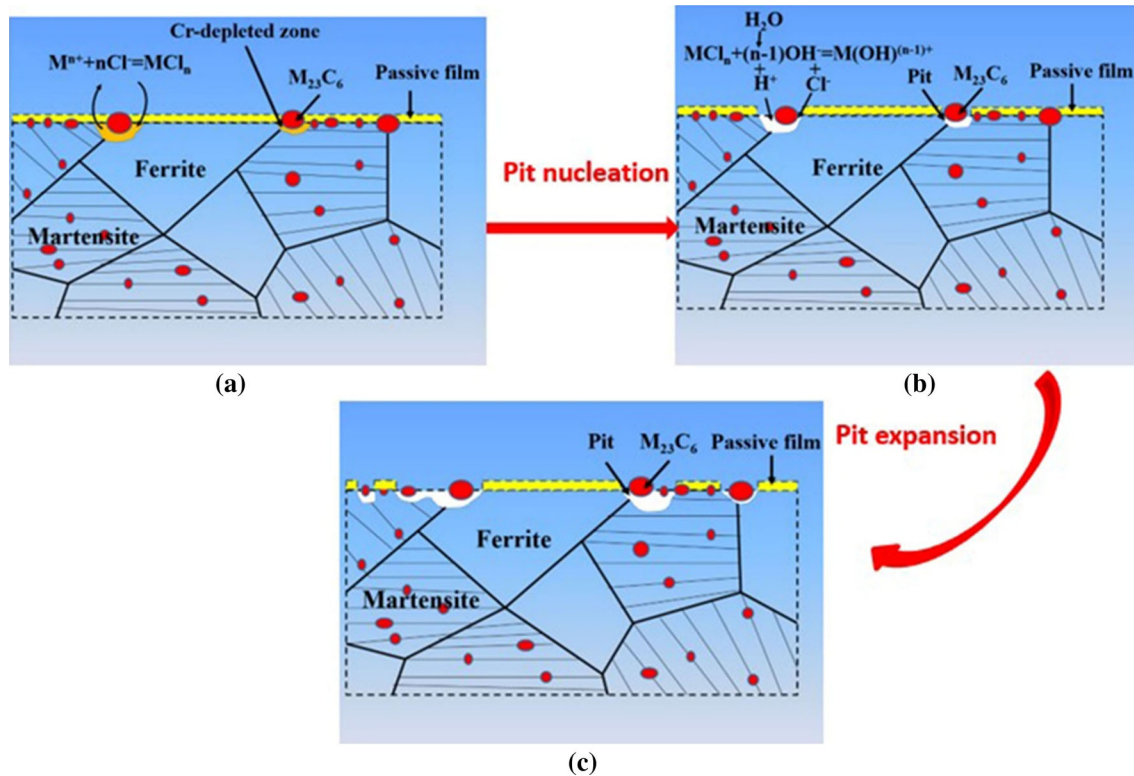


Fig. 13—Schematic illustration of the effect of nano-sized $M_{23}C_6$ carbides and nano-sized $M_{23}C_6$ carbides on the pitting behavior of the ferritic-martensitic steel: (a) sample; (b) pit nucleation; (c) pit expansion.

Table IV. The Relationship Between Precipitates and Electrochemical Corrosion Behavior

Heat Treatment Temperature (°C)	Size of Precipitates at F/M Phase Boundary (nm)	Size of Precipitates Between the Martensite Laths (nm)	Any Passivation?	Corrosion Morphology
Annealed at 950 °C and tempered at 620 °C	150	300	no passivation interval	uniform corrosion + 300 μ m corrosion pit
Annealed at 1000 °C and tempered at 290 °C	100	50	obvious passivation interval	pitting corrosion
Annealed at 1000 °C and tempered at 400 °C	150	150	weak passivation interval	uniform corrosion + pitting corrosion
Annealed at 1000 °C and tempered at 620 °C	50	150	no passivation interval	uniform corrosion + 200 μ m corrosion pit
Annealed at 1050 °C and tempered at 620 °C	30	50	no passivation interval	uniform corrosion

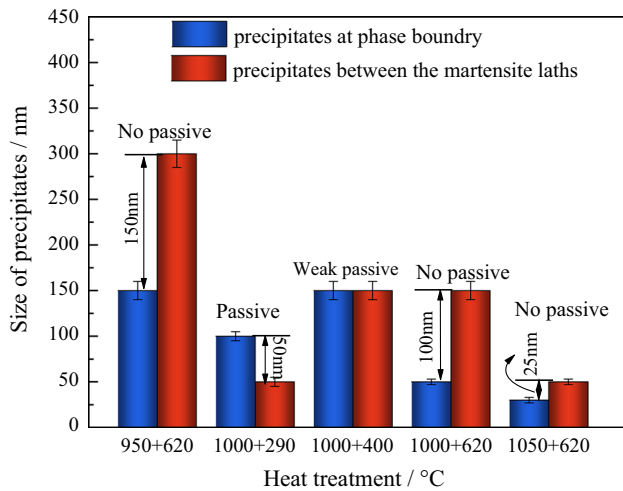


Fig. 14—The relationship between heat temperature and size of precipitates, electrochemical behavior.

V. CONCLUSIONS

- (1) The correlation between corrosion behavior of 17Cr-1Ni ferritic-martensitic stainless steel and annealing temperature was investigated by TEM, SEM, and electrochemical tests. Nano-sized chromium-rich $M_{23}C_6$ -type carbides were observed at the phase boundary and martensite laths after different heat treatment processes. With an increase in the annealing temperature, the shrunken precipitated phase results in a more protective surface film formed on steel surface, and then improved the corrosion potential and electrochemical impedance.
- (2) The effect of tempering temperatures on corrosion resistance of F/M duplex steel was also studied. When the tempering temperature was low (290 °C), carbides mainly precipitated at the boundaries because of low degree of atomic matching and higher grain boundary energy. Passive behavior was obvious and pits mainly initiated at the phase boundary. When the tempering temperature increased to 400 °C, the precipitated phase at the phase boundary and the martensite lath almost had the largest size (about 150 nm) which resulted in the worst corrosion resistance. As the tempering temperature growing higher than 400 °C, carbides gradually precipitated in the martensite laths since Cr diffused to the depleted regions and thereby healed the Cr depletion zone at phase boundary. No obvious passivation could be observed from polarization curve, and uniform corrosion occurred in martensitic region.

ACKNOWLEDGMENTS

This work was supported by the National Key Research and Development Program of China (No. 2017YFB 0702300), National Natural Science

Foundation of China (No. 51671029), and the Fundamental Research Funds for the Central Universities (No. FRF-TP-17-002B).

REFERENCES

1. Y. Kayali and B. Anaturk: *Mater. Design*, 2013, vol. 46, pp. 776–83.
2. A. Bag, K.K. Ray, and E.S. Dwarakadasa: *Metall. Mater. Trans. A*, 1999, vol. 30A, pp. 1193–1202.
3. M. Bellavoine, M. Dumont, J. Drillet, V. Hébert, and P. Maugis: *Metall. Mater. Trans. A.*, 2018, vol. 49A, pp. 2865–75.
4. S. Gündüz: *Mater. Lett.*, 2009, vol. 63, pp. 2381–83.
5. A. Neville and T. Hodgkiss: *Corros. Sci.*, 1996, vol. 38, pp. 927–56.
6. S. Qu, X. Pang, Y. Wang, and K. Gao: *Corros. Sci.*, 2013, vol. 75, pp. 67–77.
7. F.U. Yan: *Acta Metall. Sin.*, 2005, vol. 41, pp. 302–06.
8. Y.Z. Shen, Z.X. Shang, Z.Q. Xu, W.W. Liu, X. Huang, and H. Liu: *Mater. Charact.*, 2016, vol. 119, pp. 13–23.
9. H.W. Hayden and S. Fwreen: *Metall. Trans.*, 1970, vol. 1, pp. 1955–59.
10. K.M. Adhe, V. Kain, K. Madangopal, and H.S. Gadiyar: *J. Mater. Eng. Perform.*, 1996, vol. 5, pp. 500–06.
11. G.C. Palit, H.S. Gadiyar, and V.C. Kain: *Corrosion*, 1993, vol. 49, pp. 977–91.
12. V. Kain, G.C. Palit, S.S. Chouthai, and H.S. Gadiyar: *J. Electrochem. Soc.*, 1989, vol. 38, pp. 50–54.
13. K. Chandra, V. Kain, and R. Tewari: *Corros. Sci.*, 2013, vol. 67, pp. 118–29.
14. C.J. Park, V.S. Rao, and H.S. Kwon: *Corrosion*, 2005, vol. 61, pp. 76–83.
15. V. Vigna, S. Ringeval, S. Thiébaud, K. Tabalaiev, C. Dessolin, O. Heintz, Heintz, F. Herbstac, and R. Chassagnonac: *Corros. Sci.*, 2014, vol. 85, pp. 42–51.
16. S.K. Bonagani, V. Bathula, and V. Kain: *Corros. Sci.*, 2018, vol. 131, pp. 340–54.
17. B. Tang, L. Jiang, R. Hu, and Q. Li: *Mater. Charact.*, 2013, vol. 78, pp. 144–50.
18. R. Jones, V. Randle, and G. Owen: *Metall. Mater. Trans. A.*, 2008, vol. 496A, pp. 256–61.
19. T.N. Prasanthi, C. Sudha, V.T. Paul, N.S. Bharasi, S. Saroja, and M. Vijayalakshmi: *Metall. Mater. Trans. A.*, 2014, vol. 45A, pp. 4220–34.
20. S. Pahlavan, S. Moazen, I. Taji, K. Saffar, M. Hamrah, M.H. Moayed, and S.M. Beidokhti: *Corros. Sci.*, 2016, vol. 112, pp. 233–40.
21. P.P. Sarkar, P. Kumar, M.K. Manna, and P.C. Chakraborti: *Mater. Lett.*, 2005, vol. 59, pp. 2488–91.
22. Y. Zhao, W. Zhang, Z. Liu, and G. Wang: *Mater. Sci. Eng. A*, 2017, vol. 702, pp. 279–88.
23. T.H. Lee, Y.J. Lee, S.H. Joo, H.H. Nersisyan, K.T. Park, and J.H. Lee: *Metall. Mater. Trans. A.*, 2015, vol. 46A, pp. 4020–26.
24. D.C. Kong, A.N. Xu, C.F. Dong, F.X. Mao, K. Xiao, X.G. Li, and D.D. Macdonald: *Corros. Sci.*, 2017, vol. 116, pp. 34–43.
25. X. Wang, Y. Li, H. Li, S. Lin, Y. Ren, and X. Wang: *J. Mater. Process. Tech.*, 2018, vol. 252, pp. 618–27.
26. L.D. Barlow and M.D. Toit: *J. Mater. Eng. Perform.*, 2012, vol. 21, pp. 1327–36.
27. Z. Xu, Z. Ding, L. Dong, and B. Liang: *Metall. Mater. Trans. A.*, 2016, vol. 47A, pp. 1–7.
28. S.Y. Lu, K.F. Yao, Y.B. Chen, M.H. Wang, and X.Y. Ge: *Metall. Mater. Trans. A.*, 2015, vol. 46A, pp. 6090–6102.
29. S.Y. Lu, K.F. Yao, Y.B. Chen, M.H. Wang, X. Liu, and X. Ge: *Electrochim. Acta*, 2015, vol. 165, pp. 45–55.
30. Q. Yu, C.F. Dong, Y.H. Fang, K. Xiao, C.Y. Guo, G. He, and X.G. Li: *J. IronSteel Res. Int.*, 2016, vol. 23, pp. 1061–70.
31. H. Luo, C.F. Dong, X.G. Li, and K. Xiao: *Electrochim. Acta*, 2012, vol. 64, pp. 211–20.
32. Y.S. Choi, J.G. Kim, Y.S. Park, and J.Y. Park: *Mater. Lett.*, 2007, vol. 61, pp. 244–47.
33. C. Man, C.F. Dong, Z.Y. Cui, K. Xiao, Q. Yu, and X.G. Li: *Appl. Surf. Sci.*, 2018, vol. 427, pp. 763–73.

34. J. Jayaraj, K.R. Ravi, C. Mallika, and U.K. Mudali: *Metall. Mater. Trans. A.*, 2016, vol. 47A, pp. 1–11.
35. R.C. Ming, Y. Che, X. Dong, and X. Chao: *J. Mater. Sci. Technol.*, 2012, vol. 28, pp. 1059–66.
36. J.M. Pardal, M.R.D. Silva, I.N. Bastos, MCSD Macado and SSM Tavares: *Br. Corros. J.*, 2016, vol. 51, pp. 337–41.
37. C.T. Liu and J.K. Wu: *Corros. Sci.*, 2007, vol. 49, pp. 2198–2209.
38. S. Ningshen, M. Sakairi, K. Suzuki, and S. Ukai: *Appl. Surf. Sci.*, 2013, vol. 274, pp. 345–55.
39. Y. Fu, X. Wu, E.H. Han, W. Ke, K. Yang, and Z. Jiang: *Electrochim. Acta*, 2009, vol. 54, pp. 1618–29.
40. X.P. Ma, L.J. Wang, B. Qin, C.M. Liu, and S.V. Subramanian: *Mater. Des.*, 2012, vol. 34, pp. 74–81.
41. K. Asami, K. Hashimoto, and S. Shimodaira: *Corros. Sci.*, 1977, vol. 17, pp. 713–23.